SCIENCE CHINA
Information Sciences

• RESEARCH PAPER •

June 2026, Vol. 69, Iss. 6, 162405:1–162405:10
https://doi.org/10.1007/s11432-025-4762-8

Photo-synapses based on single-crystalline VO_2 films for in-sensor information processing

Xinjie HOU†, Xintian WANG†, Lei YIN*, Xunguo GONG, Ximeng PENG, Yao WEN, Yuchen CAI, Ruiqing CHENG* & Jun HE*

Key Laboratory of Artificial Micro- and Nano-structures of Ministry of Education, and School of Physics and Technology, Wuhan University, Wuhan 430072, China

Received 13 October 2025/Revised 3 December 2025/Accepted 15 January 2026/Published online 9 May 2026

Abstract Big data intensifies challenges in power efficiency and communication bandwidth. Neuromorphic computing based on emerging devices with intrinsic information processing capabilities enables energy-efficient, high-speed artificial neural networks, playing a crucial role in addressing limitations of traditional von Neumann architectures and attracting widespread attention. As a Mott material, VO_2 is pivotal for next-gen neuromorphic devices, with its near-room-temperature metal-insulator transition and resistance-switching properties. Here, we demonstrate that a fully light-modulated artificial synapse fabricated from single-crystalline VO_2 film could exhibit precisely tunable temporal dynamics and support biologically relevant synaptic plasticity, mimicking key adaptive behaviors of biological synapses. Based on this synapse, a three-layer artificial neural network architecture was implemented, where VO_2 photo-synapses functioned as image pre-processors to compress redundant visual information. Specifically, a 4×4 pixel image was condensed into a 4×1 vector, reducing computational load while maintaining high performance. This study highlights VO_2 photo-synapses' potential for advanced neuromorphic computing and intelligent vision systems.

Keywords photo-synapse, VO_2 film, photodetector array, in-sensor computing, information compression

Citation Hou X J, Wang X T, Yin L, et al. Photo-synapses based on single-crystalline VO_2 films for in-sensor information processing. Sci China Inf Sci, 2026, 69(6): 162405, https://doi.org/10.1007/s11432-025-4762-8

1 Introduction

The rapid development of artificial intelligence (AI) has rendered information processing efficiency increasingly critical [1–7]. Traditional computing architectures, constrained by the von Neumann bottleneck, often suffer from data transmission delays and high energy consumption when handling large datasets and complex tasks [8–17]. In contrast, biological nervous systems, particularly the human visual system, exhibit exceptional efficiency [6,18]. The human eye can swiftly detect light changes, convert optical signals into neural electrical impulses, and then execute parallel processing and rapid decision-making through neural networks, providing an energy-efficient model for new computing technologies [19–21]. Mimicking such biological computing paradigms, especially in visual processing, has thus become key to enhancing AI performance [22–25]. Utilizing optical signals can overcome speed and energy limitations of traditional electronics, offering new possibilities for creating efficient, low-power computing systems [26–28]. Recent years have seen new devices replicating biological information processing and perception, with neuromorphic devices standing out for high-speed processing, low-power computing, and high-bandwidth transmission [29–33]. These have gone beyond basic sensing and pre-processing tasks to encompass more complex applications, such as neuromorphic computing [34,35], visual information processing [36], image classification [37,38], and pattern matching [39]. Yet challenges persist, as reliance on task-specific optical control models and training methods limits their ability to perform multi-task processing and adapt to diverse applications [6]. This underscores a growing need for all-optical controlled neuromorphic devices, capable of multi-task visual processing and mimicking the human visual system to overcome complex real-time visual computing challenges [6, 40].

As a cutting-edge field in neuromorphic computing, all-optical controlled neuromorphic devices possess unique advantages [6]. Optical signals exhibit high speed, wide bandwidth, and low crosstalk; leveraging optical control to regulate these devices can overcome the speed and energy limitations of traditional electronics [41, 42]. Through

* Corresponding author (email: yin-lei@whu.edu.cn, chengrq@whu.edu.cn, He-jun@whu.edu.cn)
† These authors contributed equally to this work.

optoelectronic interactions, such devices can directly sense, process, and store optical signals while simulating neuronal dynamics and synaptic plasticity in biological nervous systems, paving the way for more intelligent, efficient computing [43]. Liu et al. reported an optoelectronic synapse with rich chemical tunability based on a p-AlGaN/n-GaN semiconductor nanowire photoelectrochemical architecture [44]. Gao et al. proposed a versatile vision sensor based on GaN/AlN ultrathin quantum-disks-in-nanowires (QD-NWs) with reconfigurable photoelectric properties to mimic biological visual behaviors [45]. VO_2 is a typical transition metal oxide that exhibits a reversible metal-insulator phase transition (MIT) close to room temperature, making it a key material for the development of novel neuromorphic computing devices [46–49]. It adopts distinct crystal structures under varying conditions: monoclinic VO_2 (M1) stable at room temperature and rutile VO_2 (R) stable at elevated temperatures, with the MIT occurring at approximately 68°C [46, 50]. This transition induces changes in both the crystal structure and band structure, alongside abrupt variations of 4–5 orders of magnitude in resistivity and near-unity shifts in infrared transmittance [48]. Notably, this transition exhibits hysteresis while retaining its reversibility [46,48]. Besides, VO_2 exhibits strong infrared absorption and efficient photothermal conversion, enabling the efficient conversion of optical energy into localized heat [51]. This ensures sensitive synaptic responses even under low optical power, addressing the high energy consumption bottleneck of traditional optical synapses.

In this work, we report a simple, fully light-modulated artificial synapse based on high-quality single-crystalline VO_2 film, which exhibits controllable temporal dynamics under both 808 and 1550 nm illumination and enables synaptic plasticity. Multiscale characterization confirmed the high crystalline quality and excellent uniformity of the VO_2 film. Building on this, we implemented a three-layer artificial neural network architecture, using VO_2 photo-synapses as image pre-processors to realize information compression capability. A 4×4 pixel image was compressed into a 4×1 vector, achieving 96% image recognition accuracy after 28 training epochs. This work demonstrates the potential of VO_2 photo-synapses for neuromorphic computation and intelligent vision systems.

2 Experimental section

Film growth and characterizations: Single-crystalline VO_2 films were grown on c-plane sapphire substrates using magnetron sputtering, with a base vacuum pressure below 1×10^{-7} Torr. During growth, the substrate temperature was set to 500°C, sputtering power to 100 W, and argon-oxygen flow ratio to 10:1, while the chamber pressure was maintained at 3 mTorr. Surface morphology of VO_2 films was characterized using OM (Olympus BX51M) and SEM (Zeiss Sigma 300). Crystal structure and composition were analyzed via XRD (Thermo Scientific ESCALAB 250Xi), Raman spectroscopy (Horiba equipped with a 532 nm excitation laser), and HAADF-STEM (JEM-NEOAR) equipped with EDS. XPS was conducted using an ESCALAB 250Xi.

Device fabrication and measurements: Electrode patterns were defined by UV lithography (TuoTuo Technology), followed by thermal evaporation of Cr/Au (10/50 nm) electrodes. For fabricating 2-inch device arrays, Ar/CF_4 RIE was employed to pattern the epitaxial VO_2 film into a 12 μm×25 μm microplate array, with photoresist as a mask. Source and drain regions were defined using UV photolithography, followed by thermal evaporation of 5/50 nm Cr/Au to form the source and drain electrodes. Electrical and optoelectronic measurements were performed using a probe station (Lakeshore, TTP4) equipped with a vacuum pump and liquid-nitrogen cooling system. Electrical parameters were analyzed with a B1500 semiconductor parameter analyzer. All device measurements were conducted under high vacuum ($\sim10^{-6}$ Torr) to avoid interference from air.

3 Results and discussions

Figure 1(a) shows the scanning electron microscopy (SEM) image and photograph of a 4-inch VO_2 film grown on the c-plane sapphire substrate, revealing a smooth surface morphology. The corresponding energy-dispersive X-ray spectroscopy (EDS) maps confirm the homogeneous distribution of V and O across the film (Figure 1(b)). X-ray photoelectron spectroscopy (XPS) was utilized to further characterize the film's chemical state. As shown in Figure S1, the V $2p_{3/2}$ doublet peaks at 515.3 and 516.2 eV are assigned to V^{3+} and V^{4+} states, respectively, while the O $1s$ peak at 530.0 eV corresponds to V-O bonds. Ultraviolet-visible (UV-Vis) absorption spectroscopy was conducted to determine the optical properties of VO_2 (Figure S2(a)). The corresponding Tauc plots indicate a bandgap of 0.65 eV for VO_2 (Figure S2(b)). X-ray diffraction (XRD) was performed to clarify the crystalline structure. The results (Figure 1(c)) show, aside from the sapphire (006) peak, only the monoclinic VO_2 (M-VO_2) phase (020) peak at 39.8°, confirming the film's high purity and superior crystallographic quality with no impurity phases or misorientations.

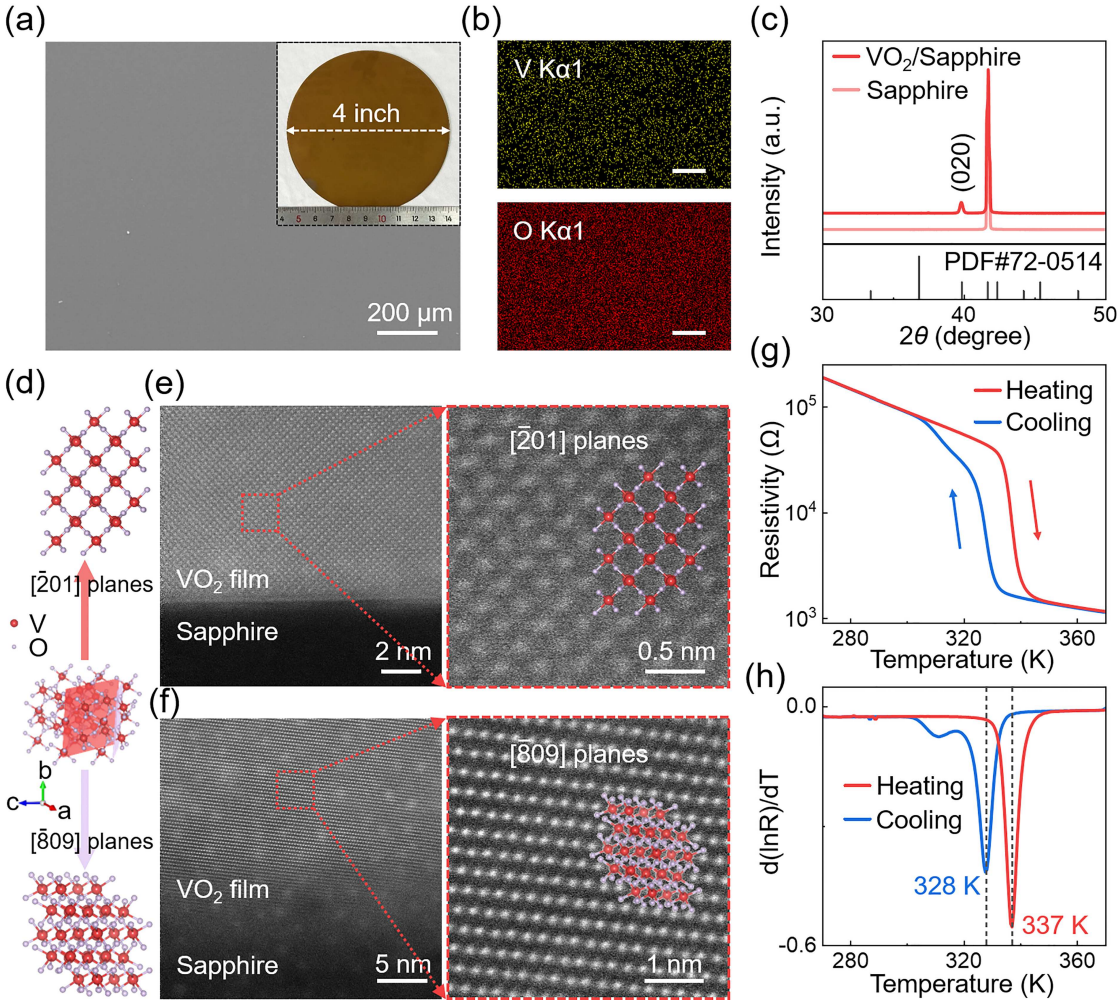

Figure 1 (Color online) Multiscale characterization of single-crystalline VO_2 film. (a) SEM image of VO_2 film on the c-plane sapphire substrate. Inset, photograph of a 4-inch VO_2 film. (b) The corresponding EDS images of the VO_2 film. (c) XRD pattern of the epitaxial VO_2 film on c-plane sapphire substrate. (d) Crystal structure diagrams of VO_2. The red shadow represents the $(\bar{2}01)$ lattice plane, while the purple shadow represents the $(\bar{8}09)$ lattice plane. Cross-sectional HAADF-STEM images at the VO_2/sapphire heteroepitaxy interface, corresponding to (e) the $[\bar{2}01]$ and (f) $[\bar{8}09]$ lattice planes of VO_2, respectively. (g) Resistivity of VO_2 as a function of temperature. (h) Logarithmic derivative plot of resistance for the VO_2 device versus temperature.

To further elucidate the structure of the VO_2 film, cross-sectional high-angle annular dark-field scanning transmission electron microscopy (HAADF-STEM) was employed. Figure 1(d) depicts the crystal structure of M-VO_2, with top and bottom panels showing projected planes along the $[\bar{2}01]$ and $[\bar{8}09]$ direction, respectively. Figures 1(e) and (f) present cross-sectional HAADF-STEM images of the VO_2/sapphire heteroepitaxial interface, corresponding to the $[\bar{2}01]$ and $[\bar{8}09]$ lattice planes, indicating the out-of-plane growth of VO_2 along [010] direction. Figure S3 shows the crystal structure of sapphire at the interface, with its out-of-plane lattice along the [001] direction. Figure S4 presents the EDS mapping of the interface, revealing a distinct boundary between the epitaxial VO_2 layer and sapphire substrate. These results confirm the epitaxial relationship of (010) VO_2 ∥ (001) sapphire, consistent with the XRD data and further validating the VO_2 film's high purity and excellent crystallinity.

The MIT behavior of the epitaxial VO_2 film was characterized using a semiconductor analyzer and physical property measurement system (PPMS). Figure S5 shows the current-voltage (I-V) curves of a two-terminal VO_2 device at different temperatures during heating and cooling cycles, respectively. Notably, an MIT occurs in the 330–340 K range during heating, whereas it happens at 320–330 K during cooling. To further determine the MIT temperature, we measured the resistivity variation of VO_2 as a function of temperature. As shown in Figure 1(g), the two-terminal VO_2 device exhibits a significant resistance change of more than two orders of magnitude across the MIT. The logarithmic derivative plot of resistance versus temperature (Figure 1(h)) enables precise determination of the transition temperature (T_C), where the T_C during the heating and cooling processes is 337 and 328 K, respectively. This exhibits a typical thermal hysteresis (the difference between T_C in heating and cooling process)

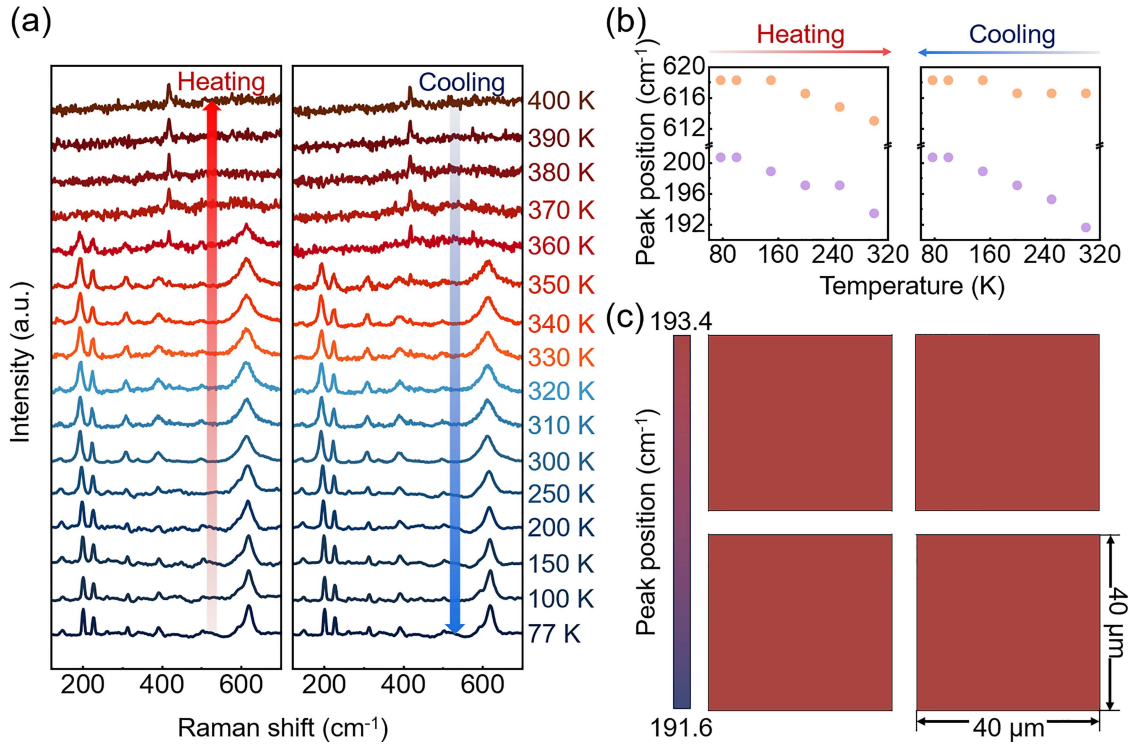

Figure 2 (Color online) Raman characterization of VO_2 film. (a) Variable-temperature Raman spectra of VO_2 film upon heating (left) and cooling (right) cycles, respectively; (b) the variation in Raman shift of the VO_2 film at 193.4 and 611.3 cm^{-1} as a function of temperature during heating (left) and cooling (right) cycles, respectively; (c) Raman mapping images of the peak position at 193.4 cm^{-1} from 4 distinct film regions.

of 9 K, a characteristic of temperature-driven first-order phase transition [46]. Figure S6 shows a photograph of the 8-inch amorphous VO_2 film on the silicon wafer. Due to its thermosensitive properties, VO_2 is well-suited for uncooled infrared detectors, which are critical for thermal imaging in various scenarios.

Systematic temperature-dependent Raman studies spanning heating and cooling cycles were conducted to elucidate the temperature-driven structural transition between the insulating monoclinic (M) and metallic rutile (R) phases in VO_2 film. As depicted in Figure 2(a), at room temperature (300 K), all Raman peaks, including those at 193.4, 224.2, 260.2, 310.5, 387.1, 499.9, and 611.3 cm^{-1} attributed to the A_g vibrational mode and 142.5 cm^{-1} corresponding to the B_g vibrational mode, are characteristic of the insulating M phase [46]. The absence of Raman peaks associated with other vanadium oxides further corroborates the high purity of our samples. During heating, the Raman peaks characteristic of the insulating M phase vanished at ~370 K, signifying the formation of the metallic R phase VO_2. Conversely, upon cooling, M phase Raman peaks reappeared at ~350 K, indicating the reemergence of the insulating M phase VO_2. Similar to the results of temperature-dependent resistance, the temperature-dependent Raman spectra of the VO_2 film exhibit typical thermal hysteresis. Figures 2(b) and S7 illustrate the temperature dependence of Raman shifts and full width at half maximum (FWHM) at 193.4 and 611.3 cm^{-1} for the VO_2 film during heating and cooling cycles, respectively. Notably, in the temperature range of 77–310 K, the 193.4 and 611.3 cm^{-1} peaks undergo a distinct redshift (i.e., toward lower wavenumbers) during heating and a corresponding blueshift (i.e., toward higher wavenumbers) during cooling. Meanwhile, the FWHM of the 193.4 and 611.3 cm^{-1} A_g peaks in the Raman spectra are increased during heating and decreased during cooling. The 193.4 cm^{-1} A_g peak of VO_2 is assigned to the V-V vibration mode, and the A_g peak at 611.3 cm^{-1} represents the V-O bond vibration [52, 53]. Consequently, we attribute the red shift and increase of the FWHM of 193.4 and 611.3 cm^{-1} A_g peaks during the heating process to the enlarged V-V distance along the c_R axis direction and the thermal effect of lattice expansion, respectively [54, 55]. Raman mapping of peak positions and FWHM at 193.4 and 611.3 cm^{-1} across 4 distinct film regions further confirms the VO_2 film's uniformity (Figures 2(c) and S8).

Having confirmed the high crystalline quality of the epitaxial VO_2 film on c-plane sapphire, a VO_2 device array was fabricated to characterize its electrical and photoresponse properties. First, single-crystalline VO_2 films were grown on 2-inch sapphire substrates using magnetron sputtering. Subsequently, reactive ion etching (RIE) was employed to pattern the epitaxial VO_2 film into a 12 μm×25 μm microplate array, with photoresist serving as a

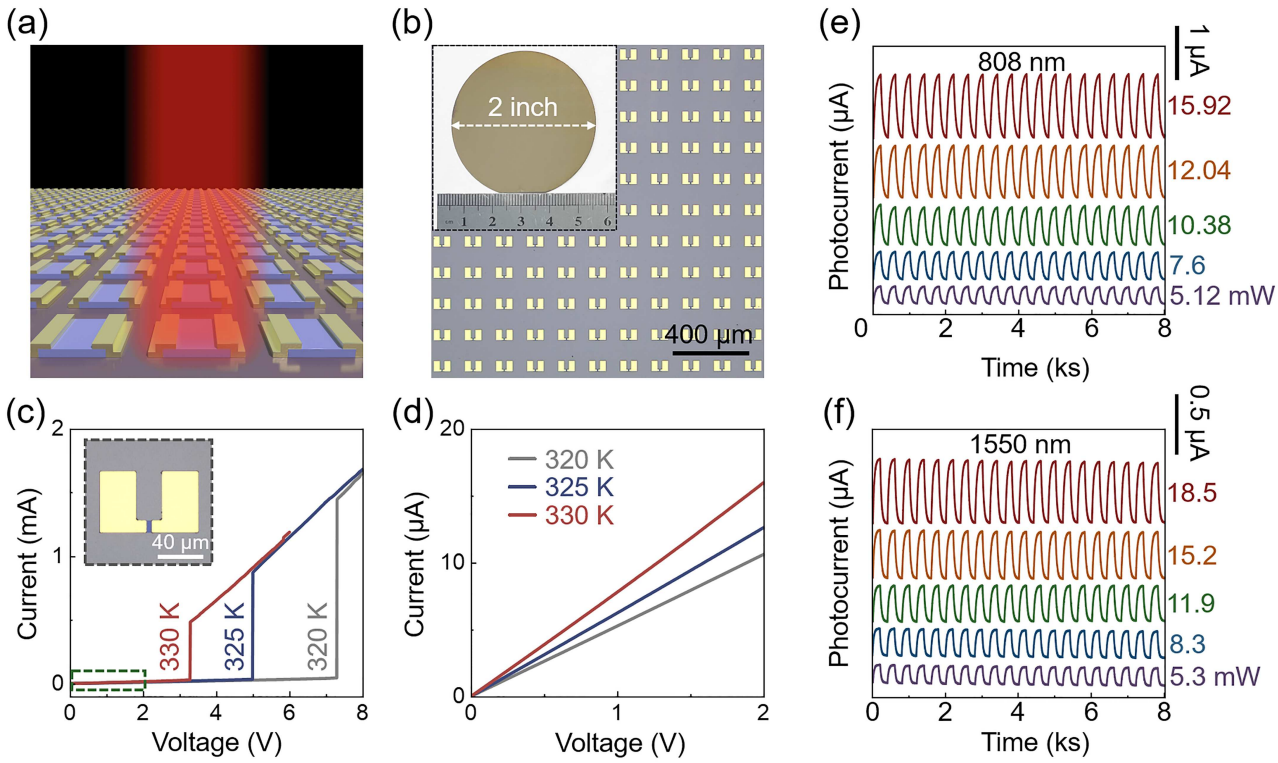

Figure 3 (Color online) Electrical and photoresponse properties of VO_2 device array. (a) Schematic diagram and (b) OM image of VO_2 device array. The inset in (b) depicts the photograph of a 2-inch VO_2 device array on the c-plane sapphire substrate. (c) Typical I-V characteristics of the VO_2 device at 320, 325, and 330 K. The inset shows the magnified view of the VO_2 device, with its channel length and width measuring 5 and 12 μm, respectively. (d) Magnified view of the green dashed box in (c). Time-dependent photoresponse of the VO_2 device with different light intensities at wavelengths of (e) 808 and (f) 1550 nm, respectively. Bias voltage is 1 V.

mask. Metal contact patterns were defined by UV lithography, followed by thermal evaporation of Cr/Au (5/50 nm) electrodes. More details about the array fabrication are available in Section 2. Figures 3(a) and (b) present the schematic diagram and optical microscope (OM) image of the 2-inch VO_2 device array, which consists of 28862 devices and achieves a high density of 1424 devices per cm^2. The corresponding channel length and width are 5 and 12 μm, respectively. To confirm the reliability and generalizability of the VO_2 device array, we conducted electrical characterizations of 15 independent VO_2 devices fabricated under the same experimental conditions (Figure S9). The results demonstrate excellent consistency across all devices. Specifically, the average conductance of the 15 devices was 4.501 μS, and the variance value was determined to be 0.056 μS. Figure 3(c) exhibits the typical current-voltage (I-V) characteristics of the VO_2 device at 320, 325, and 330 K. A magnified view of the green dashed box in Figure 3(c) is provided in Figure 3(d). Notably, the VO_2 device exhibits an electric field-induced MIT (E-MIT) behavior, accompanied by a significant resistance change exceeding two orders of magnitude across the transition. Additionally, the threshold voltage ($V_{\rm th}$) shifts toward lower values as temperature increases. Such phenomena are likely attributed to current-induced Joule heating effect, which can trigger both electrical and structural phase transitions in VO_2 devices [47]. By applying a large bias voltage (>5 V), we further observed that the VO_2 device exhibits a light-induced MIT behavior (Figure S10).

Figures 3(e) and (f) exhibit the time-dependent photoresponse characteristics of the VO_2 device under 808 and 1550 nm illumination with varying light intensities. It can be seen that the device exhibits a highly stable and reversible optical switching behavior. Meanwhile, its conductivity exhibits a sustained increase under illumination, and does not immediately revert to its pre-illumination dark-state level once the light source is removed. Such behaviors are attributed to the intrinsic photothermal effect of VO_2 [51]. Specifically, infrared light at 808 and 1550 nm is efficiently absorbed by VO_2, which induces localized heating and thereby modulates the resistivity of VO_2. To better evaluate the devices' photoresponse performance, responsivity (R) and specific detectivity (D^*) at 808 and 1550 nm were calculated (Figure S11(a)). These parameters are derived using $R = I_{\rm ph}/PS$ and $D^* = I_{\rm ph}S^{1/2}/PS(2qI_{\rm dark})^{1/2}$, where $I_{\rm ph}$ is the photocurrent ($I_{\rm ph} = I_{\rm light} - I_{\rm dark}$, $I_{\rm light}$ and $I_{\rm dark}$ are currents with and without illumination, respectively), P is incident light intensity, S is the device active area, and q is the elementary charge [56]. Under 808 nm illumination (P = 12.04 mW), the VO_2 device achieves a maximum R and D^* of

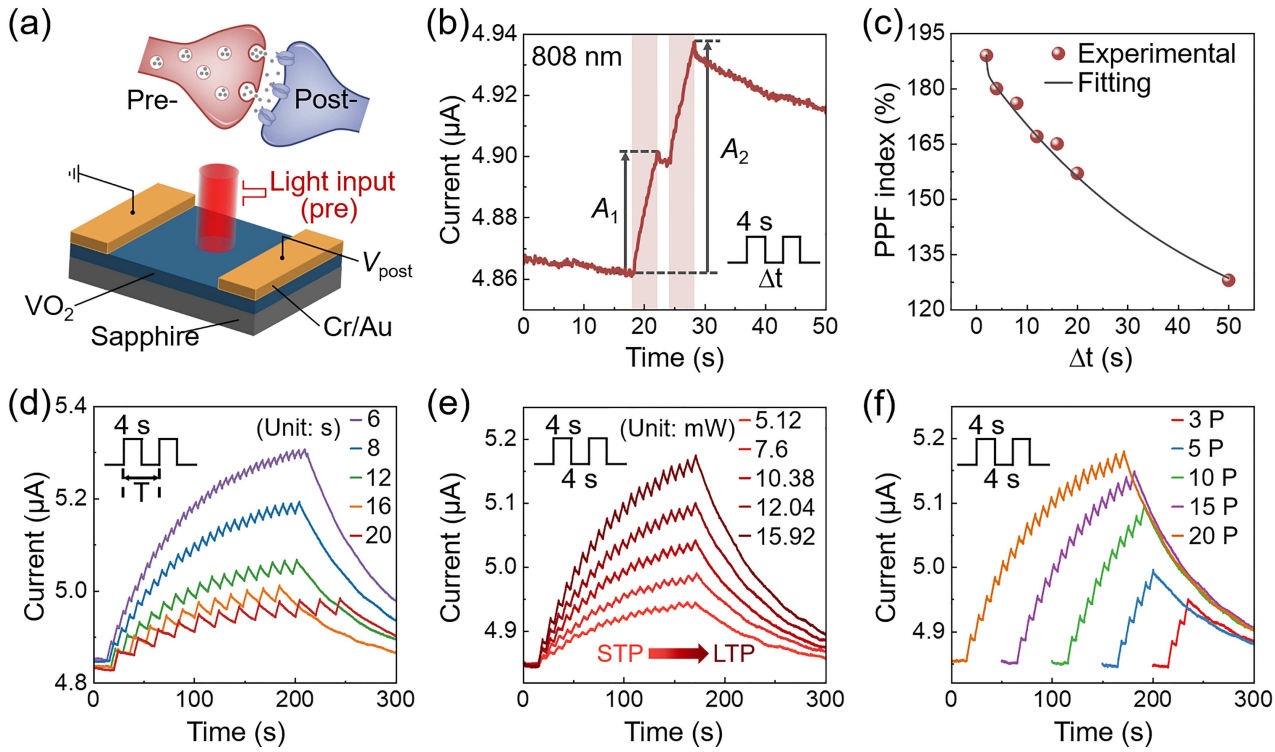

Figure 4 (Color online) Photo-synapse properties of VO_2 device. (a) Schematic diagram of biological synapses and VO_2-based photo-synapses. (b) Light-induced PPF behavior of VO_2 photo-synaptic device. (c) Dependence of the PPF index on pulse interval (from 2 to 50 s) between two 808 nm pulses, fitted by a double exponential decay function. (d) EPSC triggered by a train of optical pulses with period ranging from 6 to 20 s. And the pulse width is 4 s. (e) EPSC induced by a train of optical pulses with different optical power densities ranging from 5.12 to 15.92 mW. (f) EPSC induced by a train of optical pulses with different numbers of pulses (3, 5, 10, 15, 20).

358 mA·W^{-1} and 8.77×10^8 Jones. At 1550 nm, the maximum R and D^* reach 337 mA·W^{-1} and 8.76×10^8 Jones under 18.5 mW incident intensity. These values exceed those of previously reported SnSe-based photodetectors, likely due to the high crystalline quality of our VO_2 film [57]. Given the importance of extreme-environment optoelectronic properties for evaluating material applicability, we also characterized low-temperature performance. Under 80 K, the I-V curves of the VO_2 device under 808 and 1550 nm illumination with varying light intensities clearly illustrate the dependence of photocurrent on incident light intensity (Figures S11(b) and (c)).

Neurons are the fundamental structural and functional units of the nervous system, while synapses act as the functional junctions for information transmission between pre- and post-synaptic neurons or between neurons and effector cells (e.g., muscles, glands) [40]. Figure 4(a) illustrates the schematic diagram of a biological synapse and the VO_2-based photo-synapse device, where an infrared laser provides illumination and a 1 V bias is applied to measure device current. In synaptic simulations, infrared laser incidence on the VO_2 channel activates the pre-synaptic terminal, while the device current corresponds to the post-synaptic current (PSC), a measure of synaptic weight which reflects transmission efficiency between pre- and post-synaptic neurons. Here, an 808 nm infrared laser was employed as the stimulus for excitatory PSC (EPSC). As a core feature of neural systems, synaptic plasticity, which refers to dynamic changes in synaptic weight, is categorized into short- and long-term plasticity (STP/LTP) based on temporal persistence [8,40]. STP persists for shorter durations (typically milliseconds to minutes), serving as the basis for rapid information processing in neural systems; whereas LTP lasts hours to days, underpinning learning and memory. As a specific manifestation of STP, paired-pulse facilitation (PPF) is critical for recognizing and decoding time-resolved information: for two consecutive pre-synaptic light pulses, the synaptic weight change induced by the second pulse exceeds that from the first. This arises because carriers do not return to their initial state within the inter-pulse interval (Δt). We simulated the PPF behavior by applying a pair of 808 nm light pulses (4 s width) with varying Δt. The PPF index is defined as

$$\text{PPF index} = \frac{A_2}{A_1} \times 100\%, \tag{1}$$

where A_1 and A_2 represent the response currents triggered by the first and second pulses, respectively. At Δt = 2 s, the PPF index reaches a maximum of 189% (Figure 4(b)). The decay of the PPF index with Δt was fitted

using a double-exponential function:

$$\text{PPF index} = 1 + B_1 \exp\left(-\frac{\Delta t}{\tau_1}\right) + B_2 \exp\left(-\frac{\Delta t}{\tau_2}\right), \tag{2}$$

where B_1 and B_2 are initial facilitation amplitudes, τ_1 and τ_2 are the corresponding characteristic relaxation times of fast and slow decay, respectively. The experimental results and fitted curves are presented in Figure 4(c), revealing a negative correlation between the PPF effect and Δt.

Learning and memory based on STP and LTP are among the most critical functions in the nervous system. STP manifests as transient changes associated with short-term memory (STM), whereas LTP involves persistent alterations [40]. Notably, the transition from STP to LTP is a pivotal process in converting STM to long-term memory (LTM). In the VO_2 photo-synapse device, STP can be converted to LTP by modulating the frequency, intensity, and number of external light pulses. First, we examined the effects of different pulse intervals under a fixed pulse width. As shown in Figure 4(d), the pulse width was maintained at 4 s, while intervals were adjusted to 2, 4, 8, 12, and 16 s. Notably, as the pulse interval increased from 2 to 16 s, the amplitude of EPSC triggered by 808 nm light pulses decreased progressively, indicating a negative correlation between EPSC amplitude and pulse interval. Next, we investigated the relationship between EPSC amplitude and light pulse power density, with pulse width and interval fixed at 4 s and pulse number at 20. As illustrated in Figure 4(e), EPSC amplitude enlarges with increasing light pulse intensity. This phenomenon implies an STP-to-LTP transition, whose underlying mechanism is that higher pulse power density results in a stronger localized thermal effect through photothermal conversion. Finally, the number of light pulses is also a crucial factor influencing synaptic plasticity. When the device was stimulated with 3, 5, 10, 15, and 20 light pulses, EPSC amplitude increased monotonically with the number of pulses, indicating a positive correlation between the two (Figure 4(f)). Furthermore, we conducted photo-synaptic tests under 1550 nm illumination. The results demonstrate that the VO_2 device exhibits analogous photo-synaptic behaviors to those under 808 nm illumination, as shown in Figure S12, and highlight its potential for broadband infrared synaptic applications.

Feature extraction from the original images streamlines the recognition process and enhances efficiency [58]. Leveraging the nonlinear PPF of synaptic plasticity, input sequences to the VO_2 photo-synaptic device can be distinctly mapped to characteristic outputs. Subsequently, we demonstrated the use of VO_2 photo-synaptic devices as pre-processors in neural networks for information compression. The 4-bit information is encoded using a sequence of four 808 nm light pulses, with a pulse width and interval of 4 s and a light power of 15.92 mW (Figure 5(a)). The pulse train comprises four cycles, where the presence of a light pulse cycle is designated as the "1" state and its absence as the "0" state, thereby yielding 16 distinct states from 0000 to 1111. As depicted in Figure 5(b), the photocurrent decay curves vary significantly across different light pulse sequences. Correspondingly, the current at a specific time point can be selected, normalized to the range [0, 1] and used as a characteristic signature for each state. This confirms that the VO_2 device functions as an effective pre-processor for information compression (Figure 5(c) and Table S1). Here, we selected the current at 40 s as the sampling point (SMP).

Figure 5(d) illustrates the schematic process of using the VO_2 photo-synaptic device as a pre-processor, exemplified by a 4×4-pixel image of the letter "C". Each row of the image is fed into the device as a sequential pulse train, which then outputs the row-specific characteristic current via the aforementioned method. Through this approach, a 4×4-pixel image is compressed into a 4×1 vector, which is subsequently fed into a neural network with two hidden layers and one output layer for recognition. Two datasets containing the letters "C", "H", "I", and "P" were established, with sizes of 1000 and 200 for training and testing, respectively. Noise was introduced by flipping one of the 16 pixels from 0 to 1 or vice versa. Representative examples of noisy 4×4-pixel inputs and their corresponding compressed feature vectors are presented in Figure 5(e). Notably, all compressed vectors exhibit distinct profiles, forming the basis for high recognition accuracy. Figure 5(f) displays the accuracy and loss curves over 35 training epochs, with accuracy stabilizing at 96% after 28 epochs. This demonstrates the feasibility of the VO_2 photo-synaptic device for neuromorphic computation and image pre-processing.

4 Conclusion

In summary, we report a simple, fully light-modulated artificial synapse based on VO_2 films, which exhibits controllable temporal dynamics enabling synaptic plasticity. The high crystalline quality and excellent uniformity of the VO_2 film were verified through multiscale characterizations. Fundamental behaviors of artificial synapses, including EPSC, PPF, STP, and LTP were successfully simulated by employing an 808 nm infrared laser. Building on this, a three-layer artificial neural network architecture was implemented, using VO_2 photo-synapse as image pre-processors

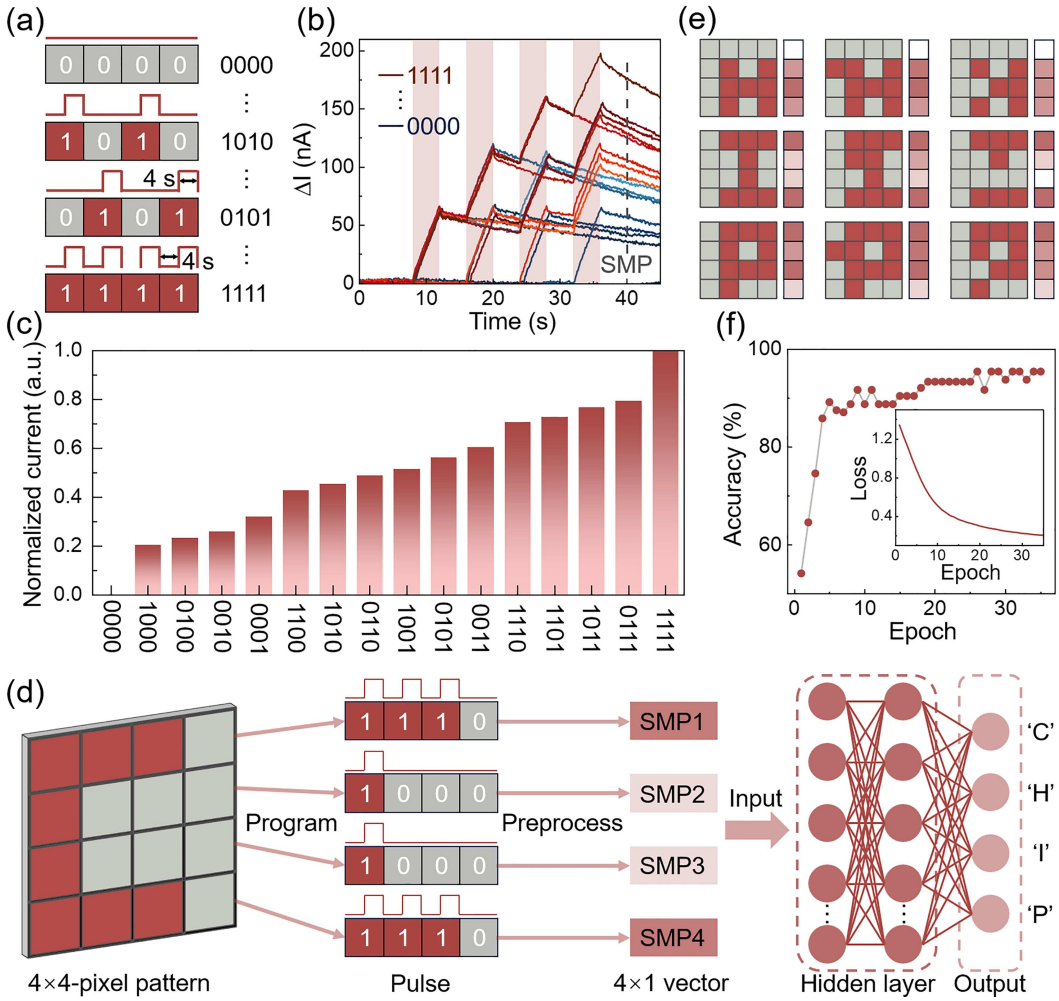

Figure 5 (Color online) Information pre-processing and compression applications of VO_2 photo-synapses. (a) 4-bit optical information is encoded using 16 sequences of four light pulses. The pulse width and interval are 4 s. (b) Photoresponse characteristics of the VO_2 photo-synapse device among different optical pulse sequences. (c) The normalized currents corresponding to the 4-bit optical information. (d) Schematic of VO_2 photo-synapses as a pre-processor to compress the input information for efficient image recognition. Here a 4 × 4 input image "C" is used as an example. Red colors at different depths refer to different current levels. (e) Other representative input images of letters "H", "I", "P" and corresponding compressed features. (f) Accuracy and loss (inset) during training.

to achieve information compression. A 4×4 pixel image was compressed into a 4×1 vector, achieving 96% image recognition accuracy after 28 training epochs. This work makes a significant contribution to the development of fully light-modulated artificial synapses and demonstrates the potential of VO_2 photo-synapse for neuromorphic computation and data pre-processing.

Acknowledgements This work was supported by National Natural Science Foundation of China (Grant Nos. U23A20364, 62274121) and Wuhan Science and Technology Major Program (Grant No. 2022013702025186).

Supporting information Figures S1–S12, Table S1. The supporting information is available online at info.scichina.com and link.springer.com. The supporting materials are published as submitted, without typesetting or editing. The responsibility for scientific accuracy and content remains entirely with the authors.

References

1 Kudithipudi D, Schuman C, Vineyard C M, et al. Neuromorphic computing at scale. Nature, 2025, 637: 801–812
2 Park H, Han J, Yim S, et al. An analysis of components and enhancement strategies for advancing memristive neural networks. Adv Mater, 2025, 37: 2412549
3 López C. Artificial intelligence and advanced materials. Adv Mater, 2023, 35: 2208683
4 Bag A, Ghosh G, Sultan M J, et al. Bio-inspired sensory receptors for artificial-intelligence perception. Adv Mater, 2024, 37: 2403150
5 Wang H, Fu T, Du Y, et al. Scientific discovery in the age of artificial intelligence. Nature, 2023, 620: 47–60
6 Yao J, Teng Y, Wang Q, et al. Advancing intelligent neuromorphic computing: recent progress in all-optical-controlled artificial synaptic devices. ACS Nano, 2025, 19: 26320–26346

7 Oh J, Ahn W, Ham A, et al. Highly reliable Bi_2O_2Se dendritic neuron enabling spatial-temporal signal processing for real-world image classification. ACS Nano, 2025, 19: 638–648
8 Cao D, Yan Y, Wang M, et al. Layered wide bandgap semiconductor $GaPS_4$ as a charge-trapping medium for use in high-temperature artificial synaptic applications. Adv Funct Mater, 2024, 34: 2314649
9 Xia Q, Yang J J. Memristive crossbar arrays for brain-inspired computing. Nat Mater, 2019, 18: 309–323
10 Choi S, Yang J, Wang G. Emerging memristive artificial synapses and neurons for energy-efficient neuromorphic computing. Adv Mater, 2020, 32: 2004659
11 Lin Y, Zhu Y, Wang F, et al. High temperature image pre-processing based on ε-Ga_2O_3 photo-synapses. Adv Phys Res, 2024, 4: 2400115
12 Duan X, Cao Z, Gao K, et al. Memristor-based neuromorphic chips. Adv Mater, 2024, 36: 2310704
13 Zidan M A, Strachan J P, Lu W D. The future of electronics based on memristive systems. Nat Electron, 2018, 1: 22–29
14 Ielmini D, Wong H S P. In-memory computing with resistive switching devices. Nat Electron, 2018, 1: 333–343
15 Park S O, Jeong H, Park J, et al. Experimental demonstration of highly reliable dynamic memristor for artificial neuron and neuromorphic computing. Nat Commun, 2022, 13: 2888
16 Yan T, Cai Y, Wang Y, et al. Near-infrared optoelectronic synapses based on a Te/α-In_2Se_3 heterojunction for neuromorphic computing. Sci China Inf Sci, 2023, 66: 160404
17 Guo Y H, Wang Y, Deng W J, et al. MoS_2 synaptic transistor with one-step manufacture. Sci China Inf Sci, 2025, 68: 112401
18 Wei B, Chen Y B, Han X T, et al. Ultra-low power MoS_2 optoelectronic synapse with wavelength sensitivity for color target recognition. Sci China Inf Sci, 2025, 68: 140406
19 Yan X, Qian J H, Sangwan V K, et al. Progress and challenges for memtransistors in neuromorphic circuits and systems. Adv Mater, 2022, 34: 2108025
20 Sanchez Esqueda I, Yan X, Rutherglen C, et al. Aligned carbon nanotube synaptic transistors for large-scale neuromorphic computing. ACS Nano, 2018, 12: 7352–7361
21 Choi C, Lee G J, Chang S, et al. Inspiration from visual ecology for advancing multifunctional robotic vision systems: bio-inspired electronic eyes and neuromorphic image sensors. Adv Mater, 2024, 36: 2412252
22 Sun B, Chen Y, Zhou G, et al. Memristor-based artificial chips. ACS Nano, 2023, 18: 14–27
23 Wang L, Wang H, Liu J, et al. Negative photoconductivity transistors for visuomorphic computing. Adv Mater, 2024, 36: 2403538
24 Jiang J, Shan X, Xu J, et al. Retina-like chlorophyll heterojunction-based optoelectronic memristor with all-optically modulated synaptic plasticity enabling neuromorphic edge detection. Adv Funct Mater, 2024, 34: 2409677
25 Zhang Y, Chen H, Sun W, et al. All-photonic synapses for biomimetic ocular system. Adv Funct Mater, 2024, 34: 2409419
26 Danial L, Pikhay E, Herbelin E, et al. Two-terminal floating-gate transistors with a low-power memristive operation mode for analogue neuromorphic computing. Nat Electron, 2019, 2: 596–605
27 Pei Y, Yan L, Wu Z, et al. Artificial visual perception nervous system based on low-dimensional material photoelectric memristors. ACS Nano, 2021, 15: 17319–17326
28 Chen Y, Xia J, Qu Y, et al. Ephaptic coupling in ultralow-power ion-gel nanofiber artificial synapses for enhanced working memory. Adv Mater, 2025, 37: 2419013
29 Han J, Deng W, Hu F, et al. 2D materials-based photodetectors with bi-directional responses in enabling intelligent optical sensing. Adv Funct Mater, 2025, 35: 2423360
30 Ilyas N, Wang J, Li C, et al. Nanostructured materials and architectures for advanced optoelectronic synaptic devices. Adv Funct Mater, 2021, 32: 2110976
31 Hong S, Cho H, Kang B H, et al. Neuromorphic active pixel image sensor array for visual memory. ACS Nano, 2021, 15: 15362–15370
32 Song H, Park W, Kim G, et al. Memristive explainable artificial intelligence hardware. Adv Mater, 2024, 36: 2400977
33 Chen Y, Gao G, Zhao J, et al. Piezotronic graphene artificial sensory synapse. Adv Funct Mater, 2019, 29: 1900959
34 Ma F, Zhu Y, Xu Z, et al. Optoelectronic perovskite synapses for neuromorphic computing. Adv Funct Mater, 2020, 30: 1908901
35 Cai Y, Yang J, Wang F, et al. Ultrasensitive solar-blind ultraviolet detection and optoelectronic neuromorphic computing using -In2Se3 phototransistors. Front Phys, 2023, 18: 33308
36 Han C, Han X, Han J, et al. Light-stimulated synaptic transistor with high PPF feature for artificial visual perception system application. Adv Funct Mater, 2022, 32: 2113053
37 Yin L, Cheng R, Pan S, et al. Engineering atomic-scale patterning and resistive switching in 2D crystals and application in image processing. Adv Mater, 2023, 35: 2306850
38 Jana R, Bhunia R, Paramanik S, et al. Conductive islands assisted resistive switching in biomimetic artificial synapse for associative learning and image recognition. Adv Funct Mater, 2024, 35: 2412804
39 Zhang Z, Wang S, Liu C, et al. All-in-one two-dimensional retinomorphic hardware device for motion detection and recognition. Nat Nanotechnol, 2021, 17: 27–32
40 Liu Z, Wang Y, Zhang Y, et al. Harnessing defects in SnSe film via photo-induced doping for fully light-controlled artificial synapse. Adv Mater, 2024, 37: 2410783
41 Yang C, Chen T, Verma D, et al. Bidirectional all-optical synapses based on a 2D Bi_2O_2Se/graphene hybrid structure for multifunctional optoelectronics. Adv Funct Mater, 2020, 30: 2001598
42 Yang R, Wang Y, Li S, et al. All-optically controlled artificial synapse based on full oxides for low-power visible neural network computing. Adv Funct Mater, 2023, 34: 2312444
43 Zhang Y, Guo Q, Duan Y, et al. The photoelectric synaptic device with sensing-memory-computing function regulated by all-optical pulse. Adv Funct Mater, 2023, 34: 2310001
44 Liu X, Wang D, Chen W, et al. Optoelectronic synapses with chemical-electric behaviors in gallium nitride semiconductors for biorealistic neuromorphic functionality. Nat Commun, 2024, 15: 7671
45 Gao Z, Ju X, Yu H, et al. Ultrathin gallium nitride quantum-disk-in-nanowire-enabled reconfigurable bioinspired sensor for high-accuracy human action recognition. Nano-Micro Lett, 2026, 18: 54
46 Li B, Xie P, Chen B, et al. Electrode-dependent and tunable sub-to-super-linear responsivity in Mott material-enabled near-infrared photodetectors for advanced near-sensor image processing. Adv Mater, 2024, 36: 2410952

47 Jeong S, Shin K H, Kim E, et al. Dual mode optoelectronic devices based on 2D single crystalline VO_2 films with controlled metallic domain regime induced variable hysteresis. Adv Opt Mater, 2024, 12: 2400196

48 Li G, Xie D, Zhong H, et al. Photo-induced non-volatile VO_2 phase transition for neuromorphic ultraviolet sensors. Nat Commun, 2022, 13: 1729

49 Feng X, Cheng R, Yin L, et al. Two-dimensional oxide crystals for device applications: challenges and opportunities. Adv Mater, 2023, 36: 2304708

50 Ma H, Xiao X, Wang Y, et al. Wafer-scale freestanding vanadium dioxide film. Sci Adv, 2021, 7: 34–38

51 Blankenship B W, Li R, Guo R, et al. Photothermally activated artificial neuromorphic synapses. Nano Lett, 2023, 23: 9020–9025

52 Geng X, Chang T, Fan J, et al. Tuning phase transition and thermochromic properties of vanadium dioxide thin films via cobalt doping. ACS Appl Mater Interfaces, 2022, 14: 19736–19746

53 Marini C, Arcangeletti E, Di Castro D, et al. Optical properties of $V_{1-x}Cr_xO_2$ compounds under high pressure. Phys Rev B, 2008, 77: 235111

54 Huang Y, Zhang D, Liu Y, et al. Phase transition analysis of thermochromic VO_2 thin films by temperature-dependent Raman scattering and ellipsometry. Appl Surf Sci, 2018, 456: 545–551

55 Nazari M, Zhao Y, Kuryatkov V V, et al. Temperature dependence of the optical properties of VO_2 deposited on sapphire with different orientations. Phys Rev B, 2013, 87: 035142

56 Yin L, He P, Cheng R, et al. Robust trap effect in transition metal dichalcogenides for advanced multifunctional devices. Nat Commun, 2019, 10: 4133

57 Yılmaz S, Başol B M, Polat İ, et al. Improvement in performance of SnSe-based photodetectors via post deposition sulfur diffusion. Sens Actuat A-Phys, 2024, 372: 115348

58 Zhang Z, Zhao X, Zhang X, et al. In-sensor reservoir computing system for latent fingerprint recognition with deep ultraviolet photo-synapses and memristor array. Nat Commun, 2022, 13: 6590